HHS Public Access

Author manuscript

Nat Neurosci. Author manuscript; available in PMC 2013 June 01.

Published in final edited form as:

Nat Neurosci. 2012 December ; 15(12): 1683–1690. doi:10.1038/nn.3255.

Orthogonal micro-organization of orientation and spatial frequency in primate primary visual cortex

Ian Nauhaus[*], **Kristina J. Nielsen**[*], **Anita A. Disney**, and **Edward M. Callaway**

Salk Institute for Biological Studies, Systems Neurobiology Laboratories

Abstract

Orientation and spatial frequency tuning are highly salient properties of neurons in primary visual cortex (V1). The combined organization of these particular tuning properties in the cortical space will strongly shape the V1 population response to different visual inputs, yet it is poorly understood. In this study, we used two-photon imaging in macaque monkey V1 to provide the first data demonstrating the 3D cell-by-cell layout of both spatial frequency and orientation tuning in large mammals. We first show that spatial frequency tuning is organized into highly structured maps that remain consistent across the depth of layer II/III, similar to orientation. Next, we show that orientation and spatial frequency maps are intimately related at the fine spatial scale observed with two-photon imaging. We find that not only do the map gradients have a striking tendency toward orthogonality, but they also co-vary negatively from cell-to-cell at the spatial scale of cortical columns.

Introduction

It has been about 50 years since Hubel and Wiesel's seminal experiments demonstrating an orderly, columnar representation of orientation (ORI) and ocular dominance preference across primary visual cortex [1,2]. Since then, optical imaging experiments have explicitly shown the two-dimensional layouts of these maps with their characteristic ORI "pinwheels" and ocular dominance "bands" [3,4]. Although it is unknown whether the existence of orderly functional maps benefits cortical processing [5], their layout and alignment are likely to put constraints on the ability of V1 to represent all stimulus features for each eye and at each region of visual space. Early on, it was suggested that the tiling of feature space in V1 is optimized to overcome this constraint [6]. Indeed, optical imaging has demonstrated that ORI pinwheels align with ocular dominance bands [7–9], and that the cortical magnification factor is lower along the axis of the ocular dominance bands [10]. Both relationships are consistent with an architecture that is optimized for uniform coverage and are currently perhaps the clearest demonstration of how multiple stimulus features are jointly encoded in V1. Spatial frequency (SF) is another important stimulus feature encoded in V1, yet the functional

[*]equal contribution by these authors

Author Contributions

I.N., K.J.N., and E.M.C. designed the research. I.N., K.J.N., A.A.D., and E.M.C. performed experiments. I.N. analyzed the data. I.N., K.J.N., and E.M.C. wrote the paper.

architecture of SF tuning is less clear than that of ORI tuning or ocular dominance. Most of the studies that mapped ORI and SF preference in cats or ferrets concluded that the maps are systematically related [11,12,13], while others reported otherwise [14,15]. Evidence on this topic in macaque V1 is much scarcer. Furthermore, the architecture of cat and ferret visual cortex is markedly different from primate V1, indicating that interactions between feature representations may not be universal.

While previous studies have presented evidence for some level of SF clustering in macaque monkey V1, the architecture of SF tuning is essentially unknown. For instance, SF tuning is often similar between nearby cells measured with extracellular electrodes [16,17,18], although the similarity is less pronounced than that for ORI [2], and there is disagreement on the degree of continuity. Similarly, a study using C-2-deoxy-glucose (DG) uptake showed that gratings of high or low SF yield patchy activation patterns [19]. Available evidence on the combined organization of SF tuning with other feature maps is even weaker, although orderly relationships seem plausible when previous observations are considered: neurons that prefer lower SF tend to cluster near the cytochrome oxidase "blobs" [16,17,18,19], blobs lie at the center of ocular dominance maps [20], and ocular dominance maps are orthogonal to ORI maps [7,8]. Taken together, this suggests a systematic relationship between ORI and SF maps, which is of particular interest with regard to the ability of V1 to efficiently represent visual space. Based on the observation that SF tuning is clustered less than ORI, it seems likely that methodological limitations have prevented a clear picture of these relationships from emerging: intrinsic signal imaging, for example, lacks single cell resolution, and single unit recordings lack sufficient sampling density. To fully address how ORI and SF are jointly represented, it is necessary to measure their organization with single cell resolution.

Here, building on previous studies using two-photon imaging of a bulk loaded calcium indicator [21] to investigate functional micro-architecture in visual cortex [22], we characterized ORI and SF tuning in layer II/III of macaque monkey V1. We find that two-photon calcium imaging allows high density sampling from large populations of macaque V1 neurons, yielding significant responses from about 94% of neurons. We quantified the degree of clustering for both parameters, based on cell pairings at different cortical distances. The normalized degree of clustering is higher for ORI than SF tuning, however both show significant clustering. The substantial clustering of ORI tuning is a reflection of its organization into precise compartments with well-defined borders, consistent with previous findings in the cat [22]. As also suggested by the clustering metric, SF preference is clearly organized into highly structured maps that are consistent across the depth of layer II/III. Finally, we show that the ORI and SF maps are organized with respect to each other in a systematic fashion: Their smoothed contours run orthogonally to each other. Consistently, we also show that the joint distribution of their gradient magnitudes is significantly anti-correlated at the finest spatial scale.

Results

We imaged visual responses in layer II/III of monkey V1 using two-photon imaging with the calcium indicator Oregon Green BAPTA-1 AM (OGB-1). Imaging was performed at two spatial scales, which we refer to as "large-scale" and "fine-scale" imaging. To achieve large-

scale imaging, we made multiple adjacent OGB-1 injections, and imaged a V1 region of about 800 × 800 μm at a resolution of ~3 μm/pixel with a 16x objective lens (Fig. 1a). Tuning curves were computed for each pixel since the lower resolution made it difficult to separate the responses of cell bodies from that of the background neuropil. However, the large field-of-view results in a more global representation of the maps. For fine-scale imaging, we zoomed in on the maps, imaging a region of about 200 × 200 μm (~0.8 μm/pix) with a 40x objective to capture the cell-by-cell tuning organization (Fig. 1e). In this case, tuning curves were computed for each cell individually. We used different stimuli to measure ORI and SF tuning at the two imaging resolutions. For the large-scale imaging, we showed drifting gratings and quantified stimulus preferences as the center-of-mass of the tuning curves (Fig 1c,d). For the fine-scale imaging, we showed a sequence of rapidly flashed gratings [23] and calculated the expected response transient to each combination of ORI and SF, followed by subtracting the expected response to an interleaved blank. The dynamics of the transient shown in Fig. 1f are quite typical. Across our population of neurons, the average time-to-peak of the raw response to the best grating was 278 (+/− 72 std. dev.) ms, and the average full-width at half-maximum was 479 (+/− 237 std. dev.) ms. Tuning curves were taken at the time-to-peak and fit with a function to characterize their shape (Fig. 1g,h). We have previously shown advantages of using a randomized noise stimulus over drifting gratings to recover accurate tuning curves with calcium imaging [24]. Additionally, we show here that about 94% of the imaged neurons yield reliable responses to the visual stimulus, and tuning curves can be well-parameterized from about 93% of the remaining responsive neurons. A summary of the tuning parameters from this population is given in Supp. Fig. 1. Two-photon imaging in the monkey thus has clear advantages over other recording techniques in terms of its ability to measure neuronal tuning from a dense sampling of neurons in a specified anatomical location.

ORI and SF maps in layer II/III

Large-scale imaging of V1 revealed a highly structured map of SF in V1, in addition to the well-known orderly representation of ORI. As expected, the ORI maps exhibit a pinwheel structure that is consistent at both depths (Fig. 2a,b and 2e,f). Unlike ORI tuning, the layout of SF preference across V1 has been unclear. Our data clearly demonstrate substantial structure in preferred SF – low or high SF preference is clustered with smooth transitions in between – and that this structure is consistent across the two depths tested here.

To compare the level of consistency across the depth of layer II/III between the ORI and SF maps, we computed a normalized metric for map similarity at the two imaging depths. The absolute difference in preferred ORI and SF between the maps at the two depths was taken for each pixel, and then averaged across pixels. To normalize, this mean difference was then recomputed after random resampling of the two maps at independent locations. Based on this metric, the ORI maps at the two depths were ~3x more similar than the SF maps for both imaging regions (Fig. 2). These differences were significant ($p < 0.01$; bootstrap).

Cell-by-cell clustering of ORI and SF tuning

Having established an orderly representation of SF preference across V1 on a more global scale, we next studied the layout of SF preference at a finer resolution. The fine-scale

imaging mode allowed us to determine ORI and SF tuning on a cell-by-cell basis ("micro-maps"). Depth of imaging ranged from ~150 μm to ~250 μm for these maps. As previously shown in cat V1 with two-photon imaging [22], our data confirm that ORI pinwheels are highly organized in the primate (Fig. 3a). Consistent with the results of our large-scale imaging experiments, SF preference also progresses continuously over the localized patch of neurons (Fig. 3b,g,l). However, it appears that SF maps exhibit more scatter than the ORI maps.

We quantified how strongly ORI and SF preference were clustered across neurons by computing a clustering metric, *C(d)*. This metric takes the expected tuning similarity between cell pairings separated by a given cortical distance *d* (Fig. 4a,b), and then normalizes by the local map statistics computed by random resampling. $C(d) > 1$ or $C(d) < 1$ indicates that two cells separated by *d* microns are likely to have tuning more similar or different than the average resampled pair, respectively. Resampling was performed two ways: In the first case, randomly selected cell pairs came from the same imaging region, which captured the level of clustering within imaging regions (~200×200 μm). In the second case, the two neurons in each pair could be from different imaging regions, thus measuring the level of clustering relative to the entire population of imaged neurons in our data set. The analyses are based on all 735 neurons, and all ~30k neuron pairs in 10 imaging regions.

Computing the degree of clustering relative to the distribution of ORI and SF tuning in each imaging region revealed that $C(d)$ is >1 for distances less than ~100 μm and <1 for the larger distances (Fig. 4c). The gradual decline of $C(d)$ with distance reflects the map continuity that exists within these small imaging regions (~200 μm). Although the general trend of $C(d)$ is similar for ORI and SF maps, SF maps exhibit more scatter relative to the local map trend.

Fig 4d summarizes the degree of clustering relative to the overall distribution of ORI and SF tuning across all imaging regions. Under the assumption that our 10 imaging regions represent an unbiased sample of ORI and SF tuning, this is the clustering relative to the distribution of ORI and SF tuning curves in layer II/III of parafoveal V1. The spatial decay of $C(d)$ reflects the spatial scale and periodicity of the maps (e.g. at larger distances $C(d)$ may have another peak, and it will ultimately decay to 1). Although $C(d)$ decays at a similar rate for ORI and SF, $C(d)$ for ORI is scaled higher, indicating that ORI is more continuous.

$C(d)$ was computed using the correlation coefficient between pairs of tuning curves. The average of these correlation coefficients within each bin of cortical distance (Fig. 4c,d) for ORI are (0.88, 0.76, 0.64, 0.50, 0.25) and for SF are (0.84, 0.76, 0.69, 0.64, 0.57). Unlike $C(d)$, there is a tendency for the correlations to be higher for SF than ORI, which is most likely due to the fact that ORI tuning is sharper than SF tuning relative to the range of available peak locations.

Intersection of ORI and SF maps

Since our data demonstrate that ORI and SF preference are both organized in a continuous fashion across V1, the question arises how the two maps are aligned with respect to each other. We used data obtained from the large-scale imaging experiments to characterize how ORI and SF maps intersect. Fig. 5 shows the ORI and SF maps obtained from an imaging

depth that is half the distance between the imaging planes shown in Fig. 2. Prior to computing contours and gradients, the raw data was smoothed with a 2D Gaussian (σ = 25 μm). Smoothing allowed us to capture the local trend of the gradients on the spatial scale of the smoothing operator. The contours of the ORI and SF maps appear to intersect orthogonally (Fig. 5c,h). To quantify the preferred angle of intersection, we first took the difference in the phase of the two map gradients at each pixel and binned these differences into a histogram (Fig. 5d,i). Indeed, the intersection histogram for each ROI shows peaks around +/− 90°. The preferred intersection angle of the gradients was then computed as a function of the intersection histogram:

$\text{Preferred intersection angle} = angle(\sqrt{\sum_{\alpha} H(\alpha) e^{i2\alpha}})$, where $H(\alpha)$ is the histogram value as a function of the intersection angle. Note that 'α' is a direction (0° to 360°) and the 'preferred intersection angle' is an orientation (0° to 180°). The preferred intersection angles for the two imaging regions in Fig. 5 were 94° and 84°. Supp. Fig. 2 also shows 3 imaging regions from 2 additional animals that had preferred intersection angles of 95°, 79°, and 99°. A Rayleigh test showed that $H(\alpha)$ was significantly different from uniform for all regions ($p < 10^{-100}$).

To compare the spatial periodicity of the ORI and SF maps, we computed their autocorrelation as a function of absolute cortical distance. For SF, we used the Pearson correlation coefficient at each shift to compute the autocorrelation. Because ORI is a circular variable, we chose to compute the autocorrelation function of the ORI map using a coherency based metric. This metric will be +1 if the original and shifted ORI maps are the same, −1 if they are 180° apart, and 0 if they are 90° apart or independent. In both regions, the autocorrelation functions of ORI and SF maps are similar (Fig. 5e,j). Both maps have a comparable rate of spatial decay, and they are both multimodal ("periodic") with a similar distance of ~800 μm (Fig. 5e top) and ~600 μm (Fig. 5e bottom) between peaks. Similar periodicities for both SF and ORI are shown for three additional imaging regions in Supp. Fig. 2.

In addition to quantifying the orthogonality between ORI and SF in the large-scale maps (Fig. 5), we tested whether a similar trend could be detected based on the global gradient within our fine-scale imaging regions. This analysis required that we develop a metric that quantifies the axis of maximum change for each ORI and SF map by using the spatial layout of tuning curves at the discrete points of the cell bodies. To define this metric for the ORI map we first defined a function that is its main dependency: $f_\theta(\lambda) = \text{median}[(1-r_\theta)/d \mid \lambda]$. In this equation, r_θ is the correlation coefficient between the ORI tuning curve fits of two cells, d the distance between the cells, and λ the angle of the line connecting the two cells (binned). In this and following equations, θ will denote ORI, and Φ will denote SF. To compute $f_\theta(\lambda)$, we divided all cell pairs into 10° wide bins based on the angle of their connecting line, and then computed $f_\theta(\lambda)$ as the median of $(1-r_\theta)/d$ across all cell pairs within each bin centered at λ. The axis of maximum change for an ORI map (Fig. 6a) can now be defined as $A_\theta = angle(\sqrt{\sum_{\lambda} f_\theta(\lambda)\, e^{i2\lambda}})$. For SF maps (Fig. 6b), A_Φ was defined by replacing r_θ with r_Φ. Finally, the angle of intersection for each imaging region was computed

as the absolute difference between A_θ and A_ϕ (mod 90°). The distribution of these intersection angles clearly clusters at 90° (Fig. 6c).

Joint distribution of pairwise changes in ORI and SF

We also analyzed the alignment of ORI and SF maps on a cell-by-cell basis, using the data obtained in the fine-scale imaging experiments. Similar to the measurements of map continuity (Fig. 4), the analysis is based on the tuning similarity between all cell pairs across all regions of interest, computed as the correlation coefficient between the tuning fits of ORI, r_Θ, and SF, r_ϕ. We first binned the cell pairs into three cortical distances, based on the 33rd and 67th percentile of the distance distribution. Within each distance bin, we generated a scatter plot where each point compares r_Θ and r_ϕ for the cell pair. These scatter plots were smoothed with a 2D Gaussian ($\sigma = 0.01$) to create the density plots shown in Fig. 7. At the shortest cortical distance ($d < 72$ μm), the maps do not show a significant interdependence. This is most likely because they are dominated more by noise than their gradients at this scale. However, with increasing cortical distance, the relationship becomes strongly anti-correlated based on the Pearson correlation coefficient. This relationship shows that if a given pair of cells has the same tuning for ORI, they are likely to have different SF tuning, and vice versa, an observation that is consistent with the orthogonal contours determined in the large-scale imaging experiments.

For a more complete illustration of this trend within the density plot, we also computed the expected value of r_Θ as a function of r_ϕ: $E(r_\Theta|r_\phi)$. For this analysis, cell pairs within each scatter plot were divided into three bins based on their r_ϕ value, and the expected value of r_Θ was computed across all the cell pairs in each bin. Bins were constructed such that they contained equal numbers of cell pairs. In a similar fashion, we also computed $E(r_\phi|r_\Theta)$. This analysis confirms that as r_ϕ increases, the expected value of r_Θ decreases, and vice versa. In the Supplementary Material, this result is replicated by showing that the local variance of the ORI map is anti-correlated with the local variance of the SF map (Supp. Fig. 3c).

Discussion

We used two-photon Ca^{2+} imaging to study the micro-architecture of ORI and SF tuning in layer II/III of macaque monkey V1. Like ORI, SF preference has a strikingly smooth progression over the cortical surface. We quantified the cell-by-cell continuity of both ORI and SF tuning as a function of cortical distance in the horizontal dimension. Both maps showed significant continuity based on our bootstrap statistic; however, ORI maps are about twice as continuous as SF maps at the shortest distances. Using a similar metric, we also quantified the similarity of the maps at two depths separated by 100 μm. The similarity of the SF maps across depth was obvious, although statistically not quite as strong as the ORI map similarity for the same regions. Next, we examined how the ORI and SF maps are jointly represented. We first captured the alignment of the map gradients determined in large-scale and fine-scale imaging experiments, and showed that ORI and SF maps have orthogonal contours. Finally, we measured this relationship based on the pairwise comparisons of the tuning curves of individual cells. This showed that the maps have a systematically antagonistic relationship on a cell-by-cell basis.

Previous studies on SF maps

To our knowledge, this is the first study to show the precise layout and continuity of the SF map in old-world primates, as well as its alignment with the ORI map. Previous studies on the organization of SF tuning in this species are relatively sparse and have yielded inconsistent results. The first study to look for SF maps in the macaque was based on DG uptake, which demonstrated that presentation of gratings with high or low SF resulted in a patchy activation pattern across V1 [19]. However, this technique makes it difficult to quantify whether local transitions of SF preference exist. Subsequent single cell recordings lent support to clustering of SF preference, yet they came to different conclusions on the distribution and organization of SF tuning. Two studies reported gradual changes in SF preference along tangential recordings [16,18], while a third study found abrupt changes in SF preference [17]. It seems probable that a lacking consensus in the primate is simply a consequence of insufficient sampling density and spatial resolution within a map that is relatively noisy.

A number of studies have looked at SF organization in other species, with most studies focusing on the cat. As in the monkey, the evidence regarding the layout of SF preference using electrophysiology and DG uptake is unsettled. SF preference has been suggested to be organized in a laminar [25,26] or a columnar fashion [27], or to lack consistency in either direction [28]. Recording from neighboring neurons in cat visual cortex, it was found that cell pairings share similar SF tuning preference, suggesting a clustered representation of SF in area 17 [29]. However, another study using different stimuli but otherwise similar techniques did not find significant clustering of SF tuning [30]. Intrinsic signal imaging promised a more global and controlled analysis of SF organization. However, given that SF tuning is less clustered than ORI tuning based on the electrophysiology [29], it is not surprising that the imaged SF maps are weaker and exhibit a less obvious structure than the ORI maps. Some studies propose that the SF maps are divided into regions of high and low SF preference [11,31], while others support a more continuous structure [12,32,33]. In terms of the alignment of SF and ORI maps, a statistically significant relationship has been reported [11–13], yet it appears difficult to detect in most examples. Finally, the mere existence of SF maps in the cat has been called into question based largely on a reanalysis of data from these previous studies, with the claim that SF maps obtained with intrinsic imaging are an artifact of a non-specific blood vessel related response [14]. Perhaps the low signal-to-noise ratio in the SF maps acquired with intrinsic signal imaging is the root of the debate. In either case, the lack of regularity in SF organization requires that it be imaged at a cellular resolution for robust characterization.

Unique aspects of macaque monkey functional architecture

Many lines of functional and anatomical evidence indicate that V1 of macaque monkeys is quite different from cat area 17 [34,35,36,37]. For example, despite the fact that both species have prominent ORI and ocular dominance columns, features related to SF encoding are different. While both species have geniculate input channels carrying different ranges of SF (parvo- and magnocellular in the macaque versus X and Y in the cat), these are segregated at the input layer (layer IV) in macaques but not cats. Furthermore, local circuits distributing this information to more superficial layers are much more highly organized in the macaque

and have tight relationships to CO blobs. In macaque monkeys, the blobs receive a mixture of direct koniocellular input and both M and P input relayed through layers 4Cα and 4Cβ respectively [36,37]. In contrast, interblobs receive less M input from 4Cα, which has been suggested as the basis for a somewhat higher prevalence of low SF tuned cells in blobs than interblobs [16]. While blobs also correspond to lower SF in cats [31], their blobs are less prominent than in macaques and it has been suggested that their low SF preferences arise from a stronger, direct Y-cell input [31,38] rather than differences in local connectivity.

In view of the differences in circuit organization that might mediate a functional architecture for SF encoding in cats versus monkeys, it should not be surprising that the strength and regularity of any relationships between SF and other functional maps might also be different. The organization between ORI and SF maps reported from intrinsic imaging studies in cats is one of a “loose orthogonality” whereby other feature maps can also be squeezed into the architecture without sacrificing too much coverage [39]. A similar result was also shown in the ferret [13]. In contrast, we have observed a much sharper and regular association between ORI and SF maps in the macaque monkey. It remains to be determined whether this relationship would appear stronger in cats or ferrets if the more sensitive two-photon imaging methods are used, but it is likely that the tight relationship between ORI and SF maps observed here does not exist in the other species studied. This is the case for other cortical maps. For example, there is a pronounced species-dependent difference in the alignment between CO blobs and ocular dominance bands. In the macaque (and human), blobs tightly align with ocular dominance columns, yet this relationship is non-existent in squirrel monkeys and appears weak at best in the cat [5]. In addition, the relationship between ORI and ocular dominance is stronger in the monkey [8,7] than the ferret [40,41,13] and perhaps the cat as well [11]. The tight ORI-SF and ORI-ocular dominance relationships in the monkey combine to suggest a parallel alignment of SF and ocular dominance maps, which is in stark contrast to what has been shown using intrinsic imaging in other species. Such a relationship between SF and ocular dominance maps is also consistent with the alignment between blobs and ocular dominance and the (likely) alignment between blobs and SF maps. It is additionally worth noting that parallel SF and ocular dominance gradients do not necessarily imply a lack of SF coverage for each eye, as the spatial period of the ocular dominance map would be twice that of the SF map. More specifically, it suggests that the most monocular regions tend to have lower SF preference.

Concluding remarks

The importance of characterizing V1 functional maps is two-fold - to better understand how map continuity may benefit wiring efficiency yet restrict coverage [42,43] and to constrain network models on the development and mechanisms of neuronal tuning in visual cortex [44,45,46,47,48]. These research avenues will benefit from the information provided by two-photon imaging, as they will ultimately require knowledge of the cell-by-cell distribution of tuning shape within the cortical space. The systematic relationship between ORI and SF tuning we have demonstrated here, along with other recent results on the exquisite layout of tuning in highly visual mammals [22,49,50] are crucial steps toward establishing a complete picture of cortical feature maps in V1.

Materials & Methods

Animal preparation and surgery

All procedures were conducted in accordance with guidelines of the National Institutes of Health and were approved by the IACUC at the Salk Institute. We used 5 juvenile macaque monkeys (4 M. fascicularis, 1 M. radiata; age 9–18 months). Animals were anesthetized with ketamine (10mg/kg, i.m.), and pre-treated with atropine (0.04 mg/kg, i.m.). They were placed in a stereotaxic apparatus, in which initially the animal's head was rigidly held in the stereotaxic frame by ear bars, eye bars, and a palate clamp (David Kopf Instruments). Anesthesia was maintained throughout the experiment with sufentanil citrate (4 – 20 μg/kg/hr, i.v.), supplemented with isoflurane (0.5–2%) during surgeries. We additionally administered diazepam (50–100 μg/kg, i.v.) as needed. For one animal, we supplemented sufentanil anesthesia with low levels of isoflurane (around 0.5%) throughout the entire experiment. Animals were paralyzed using pancuronium bromide (0.1 – 0.2 mg/kg/hr i.v.), and artificially ventilated using a small animal respirator (Harvard Apparatus or Ugo Basile). The EKG, EEG, SpO2, heart rate, and body temperature were monitored continuously to judge the animal's health and maintain proper anesthesia levels. Dexamethasone (0.1mg/kg, i.m.) and cefazolin (25mg/kg, i.v.) were administered every 24 hours to reduce brain swelling and prevent infections.

We then attached a small metal post (about 1×2 cm) to the skull over frontal cortex using metal screws and dental cement (Grip Cement, Dentsply). For the rest of the experiment, we used this head post to hold the animal's head by connecting it to the stereotaxic apparatus. At this point, ear bars and eye bars were removed, but the palate clamp remained in place. Securing the animal's head by both head post and palate clamp helped to reduce the amount of breathing induced motion artifacts during imaging.

The skull over the occipital lobe was thinned using a drill, and a custom-made imaging well was attached over V1 (see Supp. Fig. 4). Within the well perimeter, we made small craniotomies and durotomies (about 3 × 3mm) to expose the brain. Dye was then injected as described in [24]. Briefly, we injected a solution containing 2mM of OGB and 25% SR101 in ACSF [21,51]. After dye injection, the exposed brain was covered with agarose (1.5% in ACSF; type III-A, Sigma-Aldrich) and a coverslip (World Precision Instruments). To further reduce motion artifacts, the coverslip was gently pushed down by clamps attached to the imaging well. This was sufficient to remove the majority of vertical movement. However, there was usually a significant amount of residual horizontal movement, which was corrected offline using an optical flow-based method (Supp. Fig. 5). After successful dye injections, we could often image neurons down to ~400 μm; however our data was most often collected at depths between ~140 μm and ~300 μm. After collecting sufficient data from each imaging region, or when the dye loading failed to produce well labeled neurons, we performed a new craniotomy and durotomy, and repeated the dye loading in the new location. Usually, we were able to perform about 5 craniotomies/durotomies without having to move the imaging well. Whenever we could fit no more craniotomies within the imaging well, it was moved to a new position on the skull.

Eyes were dilated with 1% atropine, and corneas protected with contact lenses. Refraction of the eyes was determined for two monitor distances (60 and 80 cm). In initial experiments, we used neural responses recorded on metal electrodes to determine the ophthalmic lenses yielding the "best" SF tuning curves. For later experiments, we instead used responses from two-photon imaging.

Two-photon microscope setup

We used the same two-photon microscope as described in [24], and fixed the excitation wavelength at 920nm. Large-scale imaging was performed using a 16x, 0.8NA objective (Nikon), fine-scale imaging experiments used a 40x, 0.8NA lens (Olympus). Technical limitations of the microscope kept us from overfilling the back aperture of the 16x objective, which reduces the effective NA. The beam size was large enough to overfill the back aperture of the 40x objective. For drifting grating experiments, images were acquired at a frame rate between 2 and 8 Hz. For flashed grating experiments, the frame rate was 16 Hz.

Visual stimuli

Visual stimuli were generated using the Psychophysics Toolbox extensions for Matlab [52,53] on a 17″ CRT monitor (1024×768) with a refresh rate of 100 Hz. The monitor was gamma corrected using a Photo Research-701 spectroradiometer. We ran a set of three preliminary stimuli to help optimize the spatial frequencies and retinotopic location of the stimulus for each imaging region. The first was a large (~60° × 60°) drifting square-wave grating stimulus at eight ORIs, which gave the preferred ORIs within the ROI. In the next experiment, we presented sine-wave drifting gratings at 5 spatial frequencies (0.5, 1.0, 2.0, 4.0, and 8.0 cyc/deg), each at 1 to 2 directions. Finally, we ran a retinotopy stimulus as described in [24]. In subsequent experiments the size of the stimulus was then kept between 5° and 6°.

In fine-scale imaging experiments, we showed a random grating noise stimulus to one eye. Each presentation randomly pooled from a set of gratings of different ORI, SF, and spatial phase. The stimulus set varied across experiments, but there were always 4 phases for each ORI and SF. The domain of ORIs and SFs were organized into Cartesian coordinates. SF was spaced either linearly or logarithmically, with the range defined by the preliminary experiments. Depending on the experiment, the stimulus was updated every 150 or 200 ms. and each trial lasted 60 sec. Gratings were shown at full contrast, and a grey screen was shown instead of a grating 5% of the time.

For large-scale imaging, we presented drifting gratings because responses are more sustained and can thus be captured with a slower scan rate, which was required to image at an acceptable resolution. Furthermore, drifting gratings were deemed adequate since we were computing the preferred ORI/SF at each pixel and less concerned about distortion of the tuning curve [24]. Drifting gratings were shown to one eye at 8 directions (45° steps) and 5 SFs (0.5 to 8 cyc/deg). All combinations of direction and SF were randomly interleaved and shown 6 to 7 times.

Computing the tuning curves

Large-Scale Imaging—The response time course of each pixel for each trial was first computed as $(F(t)- F_o)/F_o$, where F_o is the mean response to the grey screen prior to stimulus onset for the given trial. Next, each frame of the trial was smoothed with a narrow 2D Gaussian (σ = 1.5 μm). We then computed the average and standard error response time course to each stimulus at each pixel (Fig. 1a–d). Responses were averaged across all presentations of the same stimulus, and the time window from 0.2 to 3.0 sec after stimulus onset. To compute the ORI and SF tuning curves at each pixel, we averaged over SF and ORI, respectively. ORI preference was measured as the direction of the resultant of response vectors. SF preference was measured as the tuning curve's center-of-mass, after taking the log of the domain. For further analysis, the imaging region was cropped based on a signal-to-noise ratio ratio (SNR) metric. We first computed the SNR at the time-to-peak of the best stimulus, at each pixel. SNR was measured as $(\mu_{max}-\mu_{min})/(SE_{max}+SE_{min})$, where μ_{max} and μ_{min} are the mean responses to the best and worst stimulus, and SE_{max} and SE_{min} are the corresponding standard errors. Next, this "SNR image" was smoothed with a 2D Gaussian (σ = 25 μm). The cropped ROI used for analyses (Figs. 2,5) consisted of pixels with SNR > 2.

Fine-Scale Imaging—For each imaging region, we created a binary cell mask for each cell body to define the overlapping set of pixels[24]. To account for glia selectively labeled with SR101, cells were removed that were present in both the red (575 to 650 nm emission filter) and green (510 to 560 nm emission filter) channel. To compute the response of a neuron at each frame, we took the dot product between a Gaussian-smoothed (σ = 1 μm) binary cell mask and the raw image. Movement correction was implemented by shifting the location of the Gaussian prior to smoothing the mask (Supp. Fig. 6). See Supp. Figs. 7,8 for a comparison of responses at the cell body to those at the adjacent neuropil.

Prior to computing the kernels for the flashed gratings, we convolved the signal for each neuron with a difference-of-Gaussians function ($\sigma_{lowpass}$ = 50 ms; $\sigma_{highpass}$ = 5000 ms) to help remove noise. Responses from each neuron were then Z-scored within each 60 sec trial. Next, we computed the mean and standard error of the fluorescence response (in Z units) to each type of grating in the ensemble, followed by subtracting the blank response from each time course. That is, the spatio-temporal kernel is defined as $K(\mathbf{p},\tau) = E[R|\mathbf{p},\tau] - E[R|b,\tau]$. $E[R|\mathbf{p},\tau]$ is the expected response (R) given a set of stimulus parameters ($\mathbf{p}$) and time after stimulus onset (τ). $E[R|b,\tau]$ is the expected response given that a "blank" was presented. ORI tuning curves were then computed from $K(\mathbf{p},\tau)$ as follows: 1) we averaged over spatial phase, 2) took the slice at the time delay of maximum response, and finally 3) took a weighted sum over SF, where the weighting function is simply the mean of the kernel over ORI. SF tuning curves were computed in the equivalent manner, such that the weighting function in ORI is the average over SF.

The first criterion for data selection was based on whether cells responded to the optimal stimulus reliably higher than to the worst stimulus. We included cells that had $(\mu_{max}-\mu_{min})/(SE_{max}+SE_{min}) > 1$. Here, $\mu_{max} = E[R|\mathbf{p_{max}},\tau_{peak}]$, $\mu_{min} = E[R|\mathbf{p_{min}},\tau_{peak}]$, and SE_{max} and SE_{min} are the corresponding standard errors. Approximately 94% of neurons

passed this criterion. The second criterion was based on the quality of the fits to the ORI and SF tuning curves. ORI tuning curves were fit by a Gaussian, and SF tuning curves by a difference-of-Gaussians. We only included cells where both fits accounted for at least 60% of the variance, which was 93% of the cells that passed the SNR criterion. This second criterion was implemented to ensure the accuracy of our pairwise tuning similarity measurements, as they are based on the correlation coefficient between these fits.

Quantifying map similarity across depth

ORI and SF maps were obtained at multiple depths with large-scale imaging. To quantify the degree of consistency that each feature map maintains across two imaging planes separated by 100 μm in layer II/III, we computed the following statistics:

$$Depth\ Consistency_{ORI} = E[|\Delta\theta|_{resampled}]/E[|\Delta\theta|_{actual}] \quad \text{Equation 1}$$

$$Depth\ Consistency_{SF} = E[|\Delta\Phi|_{resampled}]/E[|\Delta\Phi|_{actual}] \quad \text{Equation 2}$$

The denominators are the pixel-by-pixel absolute difference between the images at the two depths ($|\Delta\Theta| = |\Theta_{depth1} - \Theta_{depth2}|$; mod 180) and SF ($|\Delta\phi| = |\log_2(\phi_{depth1}/\phi_{depth2})|$), then averaged over pixels. The numerator is the average $|\Delta\Theta|$ or $|\Delta\phi|$ from randomly sampled pixel locations at each depth (with replacement). The number of samples for each resampling trial equaled the number of pixels. If Eq 1 > Eq 2 for more than 99% of trials, then the corresponding map was deemed more consistent across depth.

Characterizing functional map continuity

We compared the functional clustering between ORI and SF maps using a normalized measure of the average tuning difference between pairs of neurons. Specifically, clustering is defined as

$$Clustering(d) = \frac{E[1 - r_{resampled}]}{E[1 - r_{actual}|d]} \quad \text{Equation 3}$$

where *d* denotes the distance between cells, *r* is the correlation coefficient between the tuning curve fits (either ORI or SF, defined 'r_Θ' and 'r_ϕ') of a cell pair, and *E* is the expected value. Thus, the denominator is the average "tuning dissimilarity" between a pair of cells separated by a particular distance. The numerator is the average tuning dissimilarity between a randomly selected pair of cells. We created the pool of randomly selected cell pairs in two ways. First, the pool was created by resampling (with replacement) cell pairs contained in the same imaging region (Fig. 4c). For each resampling trial, the number of samples from each imaging region equaled the actual number of cell pair combinations in that region. So, the total number of samples for each trial equaled $\Sigma_R n_R!/[2n_R - 2)!]$, where n_R is the number of cells in imaging region '*R*'. Second, we instead created the random pool by taking any two cell pairs (with replacement) in the entire data set of 10 imaging regions (Fig. 4d). The number of selected pairs for each trial was the same as above. For each method of

resampling, there were 1000 resampling trials. If *Clustering(d)* was either >1 or <1 for at least 99% of the resampling trials, then we concluded that the map showed significant structure at the given distance.

Characterizing the joint representation of ORI and SF

Large-Scale Imaging—ORI and SF maps were smoothed prior to computing their contours and gradients. To smooth the ORI map, we first converted it into a complex valued image. Specifically, Θ(x,y) was converted to exp(i*2*Θ(x,y)). The smoothed complex image was then converted back to ORI by taking the angle/2. For both ORI and SF maps, the smoothing operator was a 2D Gaussian with σ = 25 μm. The gradient of the smoothed ORI and SF maps were computed at each pixel, based on the tuning differences between pixels computed as described above. That is, we computed ΔΘ and Δϕ in the x and y dimensions to create real and imaginary components of complex-valued matrices. The difference in phase of the gradients was then computed as described in the Results section.

Fine-Scale Imaging—We binned cell pairs into three bins according to their cortical distance, using the 33rd and 67th percentile as the boundaries for the bins. Within each distance bin, we quantified the joint distribution of r_Θ and r_ϕ by either computing the Pearson correlation coefficient between the two values, or by computing mean and standard error for r_Θ as a function of r_ϕ or vice versa.

Autocorrelation of maps

For the large-scale maps, we computed the autocorrelation as a function of absolute cortical distance, $R(d)$. For SF maps, R was computed as the correlation coefficient between the log of the maps for a given shift, d. For ORI maps we could not use the Pearson correlation coefficient, as it is a circular variable. Instead, R was computed based on the projection of the coherency between the maps for each shift. Specifically, we first compute the coherency, $Coh(d) = E[\exp(-i2\theta_d)\exp(i2\theta)]$, which is the mean of the pixel-by-pixel product between two complex images that are a function of the ORI map, θ, given that one has been shifted by d. We then take $R_\theta(d) = |Coh(d)|*\cos[angle(Coh(d))]$ as the "correlation coefficient" for the ORI maps. This metric will be 1 if θ and θ_d are the same, −1 if they are 180° apart, and ~0 if they are 90° apart or independent. For both ORI and SF autocorrelation functions, we only take into account the pixels that overlap within the SNR defined imaging region (see above) for each shift. So, larger shifts use fewer pixels to compute R.

Supplementary Material

Refer to Web version on PubMed Central for supplementary material.

Acknowledgments

Grants

This work was supported by National Eye Institute Grants EY-010742 to E. M. Callaway and EY-019821 to I. Nauhaus.

We are grateful to Soumya Chatterjee, Kenichi Ohki, and Clay Reid for preliminary designs of the imaging chamber and for graciously helping us to get started with monkey two-photon imaging. We also thank Dario

Ringach for helpful comments on an earlier version of the manuscript. Finally, we thank Mauricio De La Parra for technical assistance with the experiments.

References

1. Hubel D, Wiesel T. Receptive fields, binocular interaction and functional architecture in the cat's visual cortex. J Physiol. 1962:106–154. [PubMed: 14449617]
2. Hubel D, Wiesel T. Receptive fields and functional architecture of monkey striate cortex. J Physiol. 1968:215–243. [PubMed: 4966457]
3. Blasdel GG, Salama G. Voltage-sensitive dyes reveal a modular organization in monkey striate cortex. Nature. 1986; 321:579–585. [PubMed: 3713842]
4. Ts'o D, Frostig R, Lieke E, Grinvald A. Functional Organization of Primate Visual Cortex Revealed by High Resolution Optical Imaging. Science. 1990
5. Horton JC, Adams DL. The cortical column: a structure without a function. Philos Trans R Soc Lond, B, Biol Sci. 2005; 360:837–62. [PubMed: 15937015]
6. Hubel DH, Wiesel TN. Functional architecture of macaque monkey visual cortex (Ferrier Lecture). Proc R Soc Lond B, Biol Sci. 1977; 198:1–59. [PubMed: 20635]
7. Obermayer K, Blasdel GG. Geometry of Orientation and Ocular Dominance Columns in Monkey Striate Cortex. J Neurosci. 1993; 13:4114–4129. [PubMed: 8410181]
8. Bartfeld E, Grinvald A. Relationships between orientation-preference pinwheels, cytochrome oxidase blobs, and ocular-dominance columns in primate striate cortex. Proc Natl Acad Sci USA. 1992; 89:11905–9. [PubMed: 1465416]
9. Crair M, Ruthazer E. Ocular Dominance Peaks at Pinwheel Center Singularities of the Orientation Map in Cat Visual Cortex. J Neurophysiol. 1997:3381–3385. [PubMed: 9212282]
10. Blasdel G, Campbell D. Functional retinotopy of monkey visual cortex. J Neurosci. 2001; 21:8286–301. [PubMed: 11588200]
11. Huebener M, Shoham D, Grinvald A, Bonhoeffer T. Spatial relationships among three columnar systems in cat area 17. J Neurosci. 1997; 17:9270–84. [PubMed: 9364073]
12. Issa NP, Trepel C, Stryker MP. Spatial frequency maps in cat visual cortex. J Neurosci. 2000; 20:8504–8514. [PubMed: 11069958]
13. Yu H, Farley BJ, Jin DZ, Sur M. The coordinated mapping of visual space and response features in visual cortex. Neuron. 2005; 47:267–80. [PubMed: 16039568]
14. Sirovich L, Uglesich R. The organization of orientation and spatial frequency in primary visual cortex. Proc Natl Acad Sci USA. 2004; 101:16941–16946. [PubMed: 15550540]
15. Kim DS, Matsuda Y, Ohki K, Ajima A, Tanaka S. Geometrical and topological relationships between multiple functional maps in cat primary visual cortex. Neuroreport. 1999; 10:2515–22. [PubMed: 10574362]
16. Edwards DP, Purpura KP, Kaplan E. Contrast sensitivity and spatial frequency response of primate cortical neurons in and around the cytochrome oxidase blobs. Vision Res. 1995; 35:1501–1523. [PubMed: 7667910]
17. Born RT, Tootell R. Spatial frequency tuning of single units in macaque supragranular striate cortex. Proc Natl Acad Sci USA. 1991; 88:7066. [PubMed: 1651492]
18. Silverman MS, Grosof DH, De Valois RL, Elfar SD. Spatial-frequency organization in primate striate cortex. Proc Natl Acad Sci USA. 1989; 86:711–715. [PubMed: 2536174]
19. Tootell RB, Silverman MS, Hamilton SL, Switkes E, De Valois RL. Functional anatomy of macaque striate cortex. V Spatial frequency. J Neurosci. 1988; 8:1610–24. [PubMed: 3367213]
20. Horton J. Cytochrome oxidase patches: a new cytoarchitectonic feature of monkey visual cortex. Philos Trans R Soc Lond, B, Biol Sci. 1984:199–253. [PubMed: 6142484]
21. Stosiek C, Garaschuk O, Holthoff K, Konnerth A. In vivo two-photon calcium imaging of neuronal networks. Proc Natl Acad Sci USA. 2003; 100:7319–7324. [PubMed: 12777621]
22. Ohki K, et al. Highly ordered arrangement of single neurons in orientation pinwheels. Nature. 2006; 442:925–8. [PubMed: 16906137]

23. Ringach DL, Sapiro G, Shapley R. A subspace reverse-correlation technique for the study of visual neurons. Vision Res. 1997; 37:2455–64. [PubMed: 9381680]
24. Nauhaus I, Nielsen KJ, Callaway EM. Nonlinearity of two-photon Ca2+ imaging yields distorted measurements of tuning for V1 neuronal populations. J Neurophysiol. 2012; 107:923–36. [PubMed: 22114159]
25. Maffei L, Fiorentini A. Spatial frequency rows in the striate visual cortex. Vision Res. 1977; 17:257–264. [PubMed: 867846]
26. Berardi N, Bisti S, Cattaneo A, Fiorentini A, Maffei L. Correlation between the preferred orientation and spatial frequency of neurones in visual areas 17 and 18 of the cat. J Physiol. 1982; 323:603–618. [PubMed: 7097587]
27. Tootell RB, Silverman MS, De Valois RL. Spatial frequency columns in primary visual cortex. Science. 1981; 214:813–815. [PubMed: 7292014]
28. Tolhurst D, Thompson I. Organization of neurones preferring similar spatial frequencies in cat striate cortex. Exp Brain Res. 1982; 48:217–227. [PubMed: 7173359]
29. DeAngelis GC, Ghose GM, Ohzawa I, Freeman RD. Functional micro-organization of primary visual cortex: receptive field analysis of nearby neurons. J Neurosci. 1999; 19:4046–64. [PubMed: 10234033]
30. Molotchnikoff S, Gillet PC, Shumikhina S, Bouchard M. Spatial frequency characteristics of nearby neurons in cats' visual cortex. Neurosci Lett. 2007; 418:242–247. [PubMed: 17400381]
31. Shoham D, Huebener M, Schulze S, Grinvald A, Bonhoeffer T. Spatio-temporal frequency domains and their relation to cytochrome oxidase staining in cat visual cortex. Nature. 1997; 6616:592–33.
32. Everson RM, et al. Representation of spatial frequency and orientation in the visual cortex. Proc Natl Acad Sci USA. 1998; 95:8334–8338. [PubMed: 9653187]
33. Xu X, Anderson TJ, Casagrande VA. How do functional maps in primary visual cortex vary with eccentricity? J Comp Neurol. 2007; 501:741–755. [PubMed: 17299757]
34. Gilbert CD. Microcircuitry of the visual cortex. Annual review of neuroscience. 1983; 6:217–47.
35. Martin KAC. Neuronal circuits in cat striate cortex. Cerebral Cortex. 1984:241–84.
36. Callaway EM. Local circuits in primary visual cortex of the macaque monkey. Annual review of neuroscience. 1998; 21:47–74.
37. Nassi JJ, Callaway EM. Parallel processing strategies of the primate visual system. Nat Rev Neurosci. 2009; 10:360–72. [PubMed: 19352403]
38. Boyd JD, Matsubara JA. Laminar and columnar patterns of geniculocortical projections in the cat: relationship to cytochrome oxidase. J Comp Neurol. 1996; 365:659–82. [PubMed: 8742309]
39. Swindale NV, Shoham D, Grinvald A, Bonhoeffer T, Hübener M. Visual cortex maps are optimized for uniform coverage. Nat Neurosci. 2000; 3:822–6. [PubMed: 10903576]
40. Issa NP, Trachtenberg JT, Chapman B, Zahs KR, Stryker MP. The critical period for ocular dominance plasticity in the Ferret's visual cortex. J Neurosci. 1999; 19:6965–78. [PubMed: 10436053]
41. White L, Bosking W, Fitzpatrick D. Consistent mapping of orientation preference across irregular functional domains in ferret visual cortex. Vis Neurosci. 2001; 18:65–76. [PubMed: 11347817]
42. Durbin R, Mitchison G. A dimension reduction framework for understanding cortical maps. Nature. 1990; 343:644–7. [PubMed: 2304536]
43. Koulakov A, Chklovskii D. Orientation Preference Patterns in Mammalian Visual Cortex:: A Wire Length Minimization Approach. Neuron. 2001; 29:519–527. [PubMed: 11239440]
44. Swindale NV. The development of topography in the visual cortex: a review of models. Network (Bristol, England). 1996; 7:161–247.
45. Ferster D, Miller K. Neural mechanisms of orientation selectivity in the visual cortex. Annual review of neuroscience. 2000; 23:441–471.
46. McLaughlin D, Shapley R, Shelley M. Large-scale modeling of the primary visual cortex: influence of cortical architecture upon neuronal response. J Physiol Paris. 2003; 97:237–52. [PubMed: 14766144]

47. Paik SB, Ringach DL. Retinal origin of orientation maps in visual cortex. Nature neuroscience. 2011; 14:919–25. [PubMed: 21623365]

48. Kaschube M, et al. Universality in the evolution of orientation columns in the visual cortex. Science (New York, NY). 2010; 330:1113–6.

49. Li Y, Van Hooser SD, Mazurek M, White LE, Fitzpatrick D. Experience with moving visual stimuli drives the early development of cortical direction selectivity. Nature. 2008; 456:952–6. [PubMed: 18946471]

50. Kara P, Boyd JD. A micro-architecture for binocular disparity and ocular dominance in visual cortex. Nature. 2009; 458:627–31. [PubMed: 19158677]

51. Nimmerjahn A, Kirchhoff F, Kerr JND, Helmchen F. Sulforhodamine 101 as a specific marker of astroglia in the neocortex in vivo. Nat Methods. 2004; 1:31–37. [PubMed: 15782150]

52. Brainard D. The Psychophysics Toolbox. Spat Vis. 1997; 12:1317–1324.

53. Pelli D. The VideoToolbox software for visual psychophysics: transforming numbers to movies. Spat Vis. 1997; 10:437–442. [PubMed: 9176953]

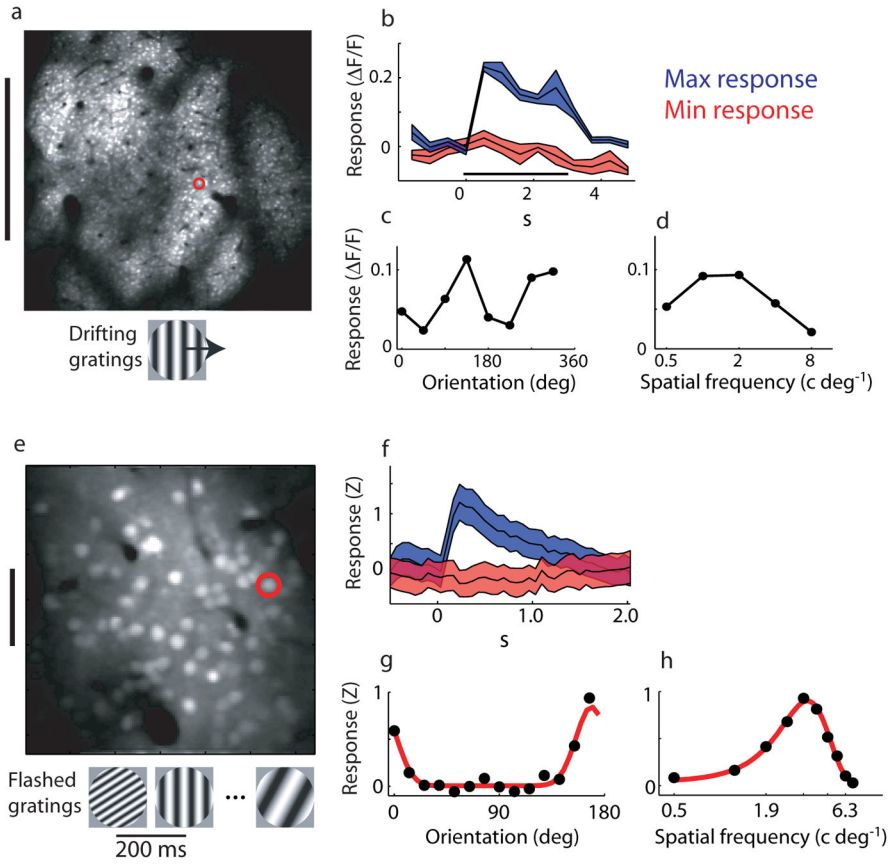

Figure 1.

Two experimental two-photon imaging paradigms. (a–d) Large-scale imaging: (a) To image a larger section of the cortex (“large scale”), we used a 16x objective lens (~ 3μm/pixel). Drifting gratings were used to measure ORI and SF tuning curves at each pixel. (b) For the pixel circled in red at left, we computed the mean and standard error time course for each combination of ORI and SF. Shown here are the time courses for the best (blue) and worst (red) combinations. The thin black line represents the stimulus presentation period. (c,d) ORI and SF tuning curves were computed by taking the mean within the stimulus presentation period. (c) ORI tuning for the pixel outlined in red in (a). (d) SF tuning curve for the same pixel. (e–h) Fine-scale imaging: (e) To measure responses of individual neurons, we imaged with higher resolution (~1 μm/pixel). Instead of drifting gratings, this stimulus paradigm employed flashed gratings shown in rapid succession. (f) Tuning curves were computed from the average transient response to each grating within our randomized flashed grating stimulus. The time courses are from the neuron circled on the left. (g,h) Raw ORI tuning and SF tuning curves (black dots) and fits (red line).

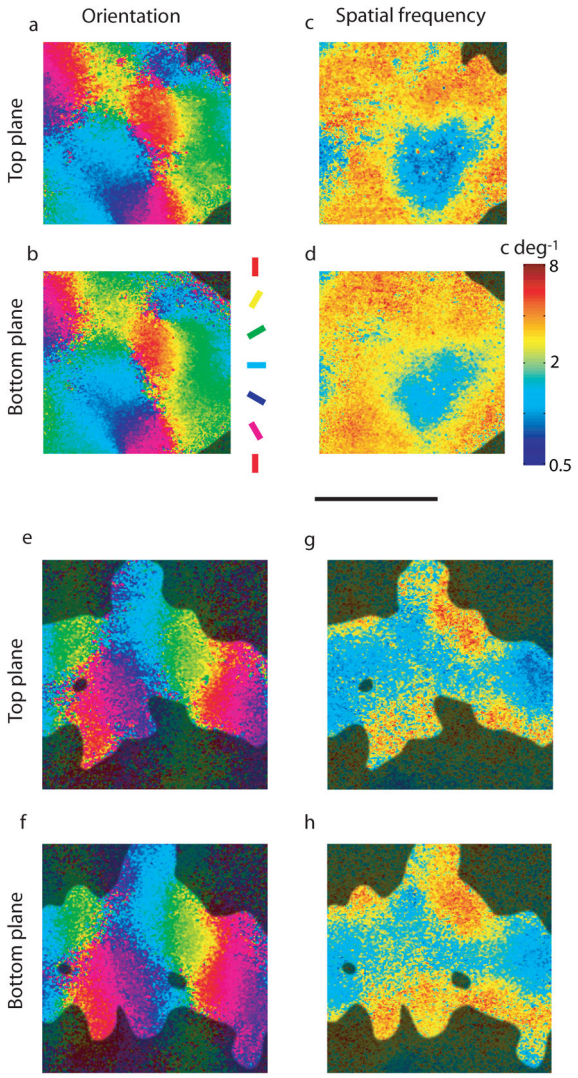

Figure 2.

Large scale imaging of ORI and SF maps at multiple depths of layer II/III for two cortical locations (top and bottom). (a,b) ORI preference maps at two cortical depths: 210 μm and 310 μm. Scale bar = 0.5 mm. (c,d) SF maps obtained from the same experiment. Both ORI and SF maps maintain a very similar structure across the two depths. Dark map regions indicate portions of the map with low SNR (Methods). (e–h) Bottom 4 panels depict a second cortical region at two depths: 180 μm and 280 μm.

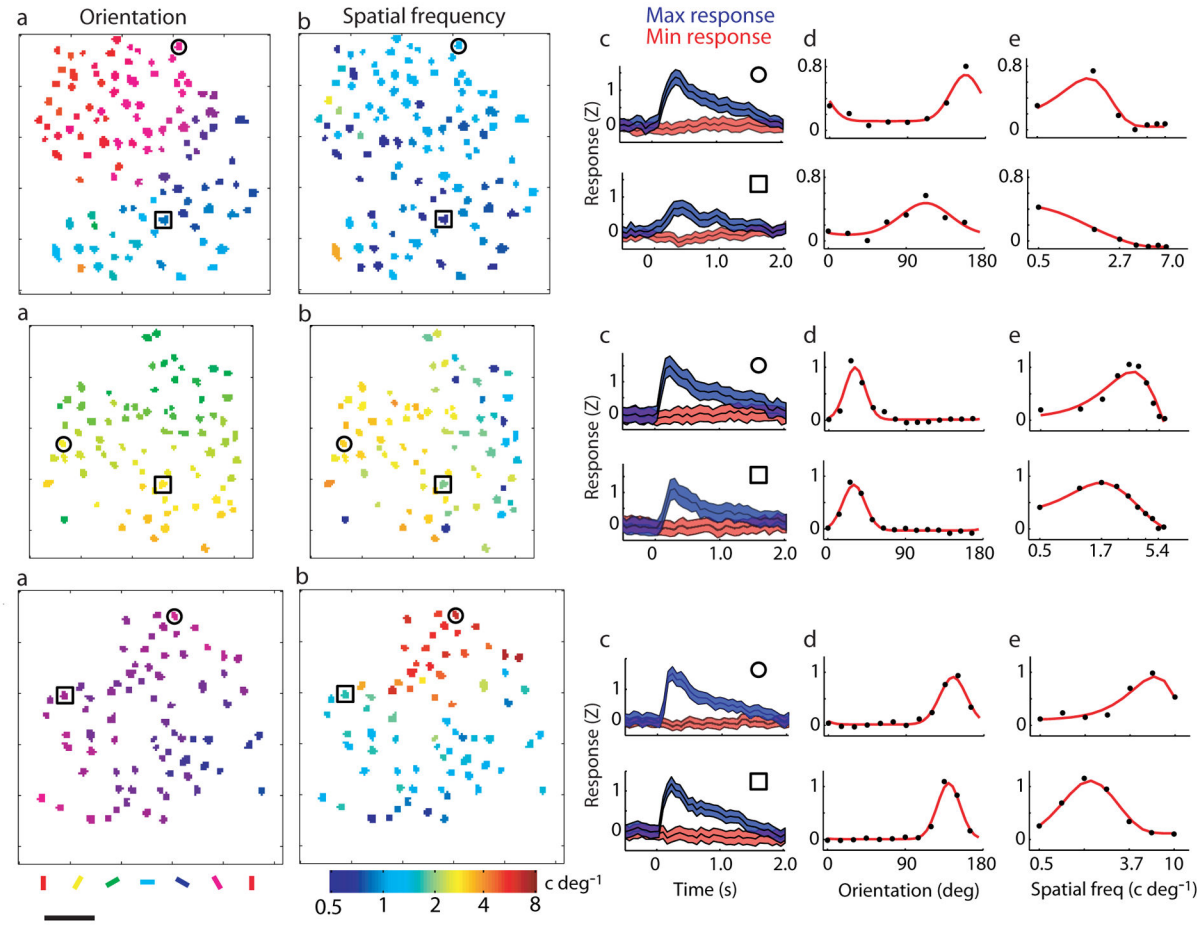

Figure 3.

Micro-maps of ORI and SF for three example regions (each row), each ~150 μm deep. Each neuron's preference for ORI (a) and SF (b) is color-coded. (c–e) For each region shown, the average responses are given for two example neurons (circle and square). (c) Mean and standard error response time course to the "best" (blue) and "worst" (red) combination of ORI and SF. ORI (d) and SF (e) tuning curves (black dots) were computed at the optimal time delay and fit with a Gaussian and difference-of-Gaussians function (red curve), respectively. (f–o) Bottom two rows depict two more cortical regions. Error bar at bottom left is 50 μm.

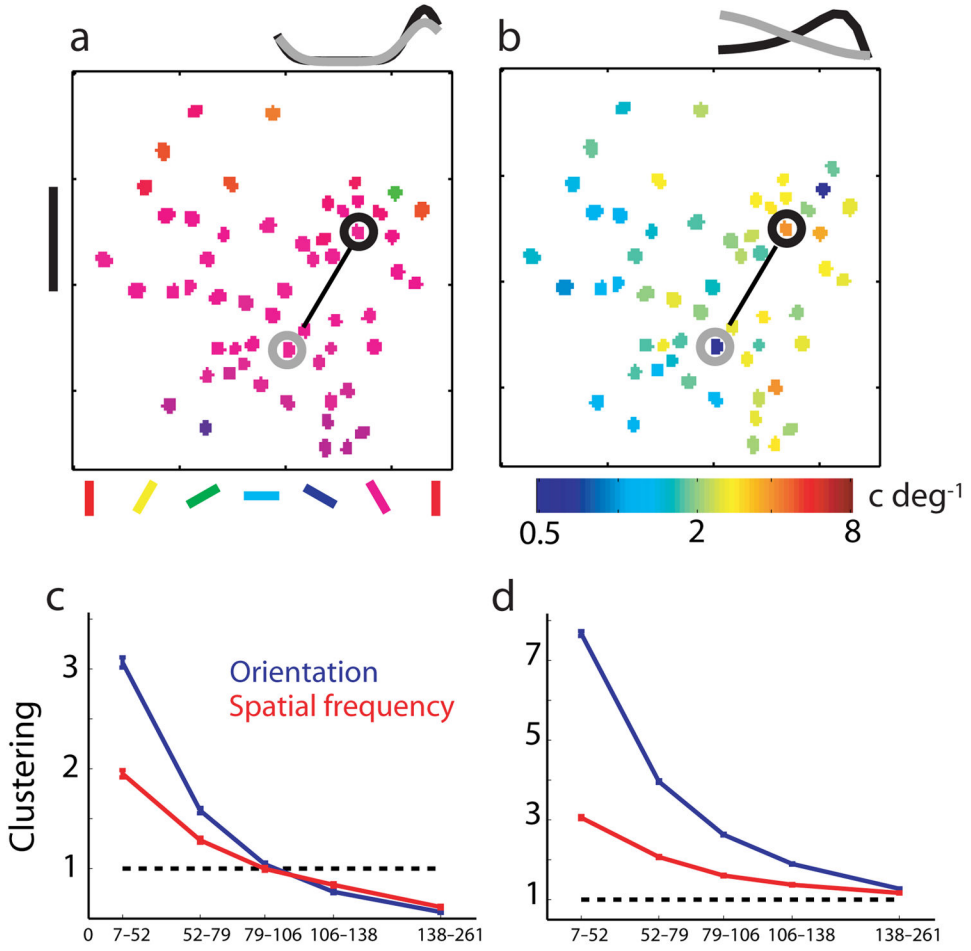

Figure 4.

Bootstrap analysis to examine clustering of micro-maps. To illustrate the pairwise analysis, we show an example cell pairing within an ORI (a) and SF (b) map (~160 μm deep). Scale bar = 50 μm. This particular pairing with a distance of ~70 μm has an ORI and SF correlation (r_Θ and r_ϕ) of 0.98 and −0.68 based on the Gaussian fits shown on top. (c) Functional clustering (y-axis) relative to the distribution of the individual imaging regions. The clustering metric is based on the average correlation coefficient across pairings within a particular distance range (x-axis), normalized by a resampled average. In this case the resampling was limited to cell pairs in the same imaging region. Each tick mark on the x-axis is located at the mean distance between pairs for the given population of pairings. Significance above or below one ("chance") was computed from multiple trials of resampling. Both maps are significantly different than one for all distances. (d) Functional clustering relative to our entire population of imaged neurons. Clustering was computed similar to (c), but resampling was between any two neurons of the entire data set. Clustering is significantly above one for all distances of both ORI and SF maps.

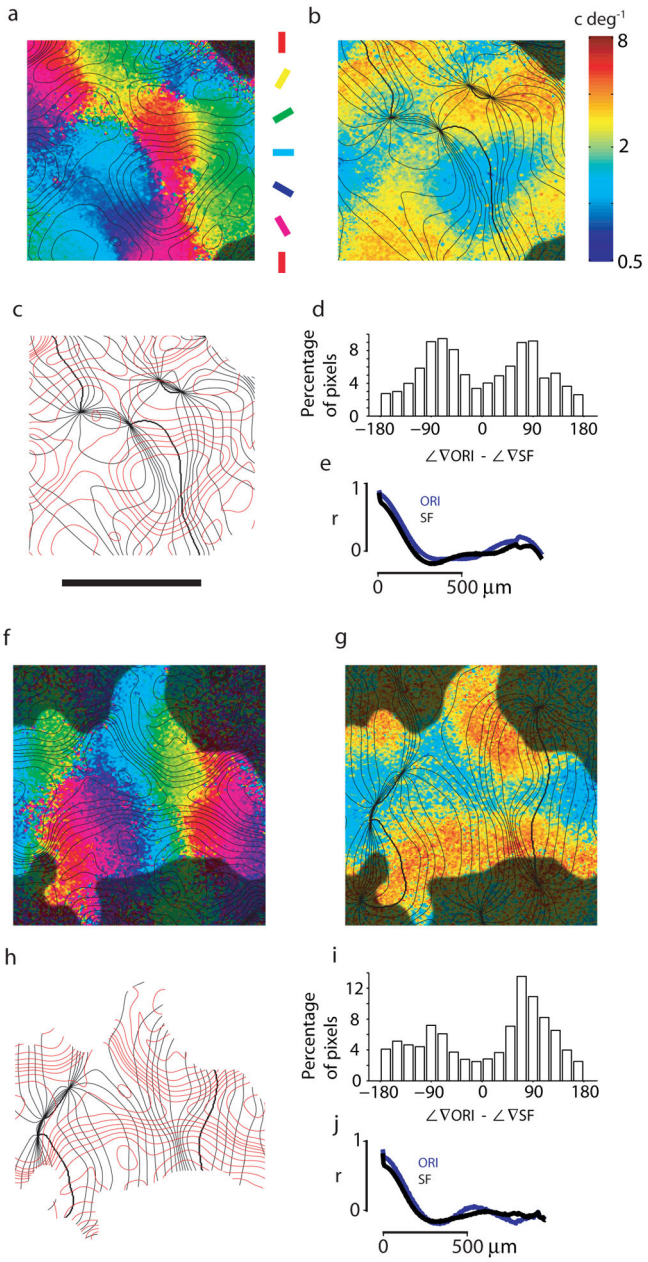

Figure 5.

Relationship between ORI and SF maps for two cortical locations, each at an imaging depth of 260 μm (top panels) and 230 μm (bottom panels). (a,f) ORI maps with the smoothed SF contours overlaid in black. (b,g) Corresponding SF maps with the smoothed ORI contours overlaid in black. (c,h) Combined ORI (black) and SF (red) contours. Scale bar = 0.5 mm. (d,i) Histograms, showing the distribution of the intersection angle between ORI and SF map gradients. The preferred intersections (94 and 84) were computed from the histograms as the angle of a weighted sum of vectors (Results). (e,j) Autocorrelation of both ORI (blue) and SF (black) maps, as a function of absolute cortical distance.

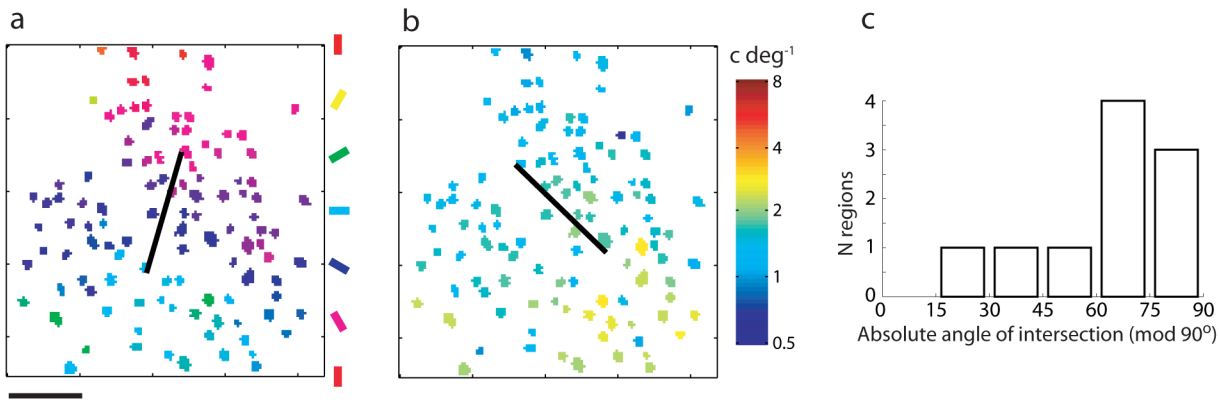

Figure 6.

Measuring the angle of intersection between micro-maps of ORI and SF. The axis of maximum change was computed for each micro-map of ORI and SF, which then gave an axis of intersection for each imaged region. An example ORI (a) and SF (b) map is shown (160 μm deep), with the computed axes overlayed in black. The intersection for this region was ~60°. (f) A histogram of intersections from 10 imaging regions is shown.

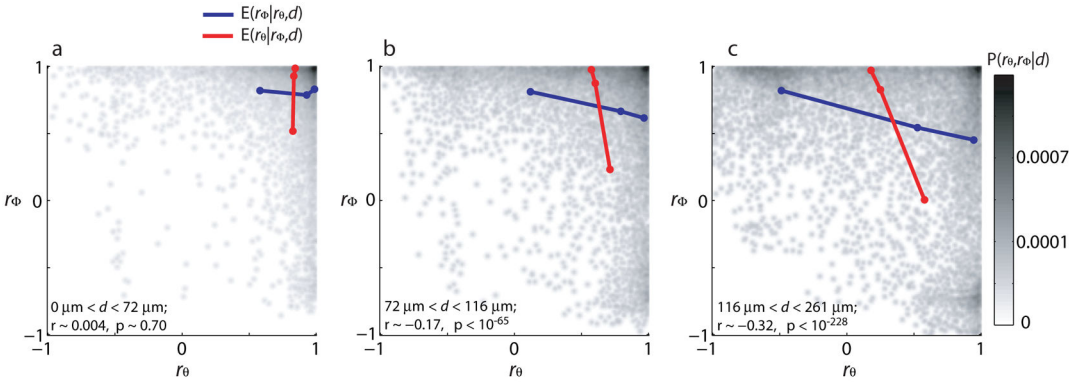

Figure 7.

Measuring orthogonality based on tuning curves of single neurons. (a–c) Joint distribution of pairwise ORI and SF tuning similarity. Similar to the analysis for "clustering" in Fig. 4, we computed the correlation coefficient between ORI (r_Θ) and SF (r_ϕ) tuning curves for all cell pairs across 9 imaging regions. Each cell pair was binned based on the 33rd and 66th percentile of cortical distance of separation. The three images are the density plots for each of the distances. The text in each inset gives the distance range for the subpopulation, along with the correlation coefficient and p-value of the scatter plot. For shorter distances (<72 µm), there is not a significant relationship between the maps (inset contains p-value of correlation in the scatter plot). However, for the other two scatter plots (>72 µm), pairwise tuning similarity is negatively correlated between the ORI and SF maps. To better illustrate the trend, we have also plotted the mean of r_ϕ (blue) and r_Θ (red), for each of three intervals on the opposing axis. Intervals were chosen to contain equal numbers of cell pairs. The standard error bars are smaller than the width of the line